Microsc. Microanal. 20, 1682–1691, 2014
doi:10.1017/S1431927614013385

Microscopy AND Microanalysis

Spectral Analysis of Irregular Roughness Artifacts Measured by Atomic Force Microscopy and Laser Scanning Microscopy

Yuhang Chen,[1,*] Tingting Luo,[1] Chengfu Ma,[1] Wenhao Huang,[1] and Sitian Gao[2]

[1]*Department of Precision Machinery and Precision Instrumentation, University of Science and Technology of China, Hefei 230026, People's Republic of China*
[2]*Division of Metrology in Length and Precision Engineering, National Institute of Metrology, Beijing 100013, People's Republic of China*

Abstract: Atomic force microscopy (AFM) and laser scanning microscopy (LSM) measurements on a series of specially designed roughness artifacts were performed and the results characterized by spectral analysis. As demonstrated by comparisons, both AFM and LSM can image the complex structures with high resolution and fidelity. When the surface autocorrelation length increases from 200 to 500 nm, the cumulative power spectral density spectra of the design, AFM and LSM data reach a better agreement with each other. The critical wavelength of AFM characterization is smaller than that of LSM, and the gap between the measured and designed critical wavelengths is reduced with an increase in the surface autocorrelation length. Topography measurements of surfaces with a near zero or negatively skewed height distribution were determined to be accurate. However, obvious discrepancies were found for surfaces with a positive skewness owing to more severe dilations of either the solid tip of the AFM or the laser tip of the LSM. Further surface parameter evaluation and template matching analysis verified that the main distortions in AFM measurements are tip dilations while those in LSM are generally larger and more complex.

Key words: atomic force microscopy, laser scanning microscopy, surface areal roughness, spectral analysis, irregular roughness artifact

Introduction

With rapid reduction of the critical dimension, many surface structures reveal novel physical and chemical properties and show promising prospects for applications in various fields of science and technology (Liu & Jiang, 2011). Surface textures at the micro- and nanoscale have been found to be closely relevant to functional performance such as wear, lubrication, wetting, and antireflection (Persson et al., 2005; Jung & Bhushan, 2006; Santos et al., 2008; da Silva et al., 2011). Consequently, surface nanometrology has emerged as a significant subject and has already drawn considerable attention. Because of the definite relationship between geometrical structure and functional capability, three-dimensional (3D) surface areal roughness characterizations, including measurement techniques and analysis methods, are especially important.

Two common procedures, instrumental measurement and quantification, are involved in surface characterization. For determining surface structure with ultrahigh resolution, popular techniques are available such as scanning electron microscopy (SEM), laser scanning microscopy (LSM), and scanning probe microscopy (SPM). SEM methods usually require a vacuum environment to achieve better performance and 3D reconstruction of the obtained image is rather complex (Bonetto et al., 2006; Kang et al., 2012). Confocal LSM measurements are obtained in a noncontact and nondestructive manner since a laser probe is employed (Hanlon et al., 2001; Yamazoe et al., 2012). In addition, current LSM techniques reach nanoscale resolution. Such features of the LSM are quite appealing. Atomic force microscopy (AFM), which belongs to the SPM family, has prominent advantages including ultrahigh dimensional resolution, numerous operation modes, easy sample preparations, and flexible working environments (Botta et al., 2008). These characteristics enable AFM to be one of the most important tools in nanotechnology (Fujita et al., 2007).

Even with high imaging resolution, quantitative evaluation of surface roughness at the nanoscale level remains very challenging. The specimen under inspection may have arbitrary structures, and the geometric interaction between the sensing probe and the sample could be excessively intricate for all of these different techniques (Hanlon et al., 2001; Chen & Huang, 2004; Kang et al., 2012; Seah, 2013). To ascertain the correctness of surface areal roughness measurements, reference structures with their topography and statistical quantities precisely controlled are required (Nemoto et al., 2009; Uchidate et al., 2011; Baršić et al., 2012; Liu et al., 2012; Chen et al., 2013; Luo et al., 2013).

Received January 20, 2014; accepted September 24, 2014
*Corresponding author. chenyh@ustc.edu.cn

To develop roughness artifacts and analysis methods, we performed comparisons of AFM and LSM measurements on a kind of digitally designed and focused ion beam (FIB) fabricated 3D structures with prescribed surface statistical quantities. Spectral characteristics, which were elucidated via power spectral density (PSD) analysis, were used. PSD offers visualization of surface geometric properties at all wavelengths. Information on the instrumental responses at different spatial frequencies can thus be obtained.

Materials and Methods

The design, fabrication, and AFM characterization of irregular roughness artifacts have been reported in our previous work (Liu et al., 2012; Chen et al., 2013, 2014). Here we briefly sketch the relevant methods with focus on the comparison of AFM and LSM measurements and the spectral analysis.

Design and Fabrication of Roughness Artifacts

It is known that a random surface can be characterized by its height distribution and autocorrelation function (ACF). Irregular surface areal roughness patterns can be designed utilizing a conventional 2D digital filter method and optimized with genetic algorithms (Wu, 2000; Liu et al., 2012). As a result, surfaces with a predetermined ACF and some fundamental statistical parameters can be efficiently simulated. The ACF is assumed to be Gaussian and is given by:

$$R(x,y) = \sigma^2 \exp\left\{-2.3\left[\left(\frac{x}{\tau_x}\right)^2 + \left(\frac{y}{\tau_y}\right)^2\right]\right\}. \quad (1)$$

In this equation, σ is the standard deviation of surface heights. τ_x and τ_y are the autocorrelation lengths in the x and y directions, respectively. The factor 2.3 means that the ACF is specified as an exponential decay with the coefficient set to reach 0.1 decrease at the autocorrelation length. It is worth mentioning that these assumptions and specifications are only for the demonstration purpose while other forms can be used flexibly (Bakolas, 2003). For the non-Gaussian surface generation, skewness and kurtosis, which are the normalized third and fourth central moments of the surface heights $\{z(x,y)\}$, can be adopted to regulate the amplitude distribution. Three kinds of artifacts were generated as prototypes, namely the roughness surfaces with negatively skewed, Gaussian, and positively skewed height distributions. The deviations between the surface statistical quantities and the corresponding expected values were controlled to be within 5%. All the surfaces have a developed area of $5.12 \times 5.12\ \mu$m and the detailed parameters are provided in the Results section.

FIB was used to fabricate the 3D structures on a silicon substrate. Compared with other approaches such as electron beam lithography (Liu et al., 2012; Chen et al., 2013) and direct laser writing (Brissonneau et al., 2012; Luo et al., 2013), FIB fabrication is capable of providing much higher resolution. The process is easier since developing and fixing procedures of photoresists are absent (Chen et al., 2014). In fabrication, the designed surface data set is transformed into a bitmap image first. The ion fluence at each pixel is subsequently evaluated according to the grayscale level, which denotes the corresponding surface height. The milling depth is precisely controlled by adjusting dwell time and repetition loops. After the pixel-by-pixel scan, while varying the fluence simultaneously, the digital roughness pattern is produced. Our fabrications were carried out on a FIB/SEM dual beam system (FEI Nova 200 Nanolab, FEI Company, Hillsboro, OR, USA). The resolution was determined to be ~7 nm at the acceleration voltage of 30 kV and beam current of 300 pA.

Atomic Force Microscopy and Laser Scanning Microscopy Characterization

The AFM measurements were performed on a commercial instrument (Bruker Innova, Bruker, Santa Barbara, CA, USA). The probe was a RTESPA-CP cantilever (Bruker Corporation, Fremont, CA, USA), which has a resonance frequency of 358 kHz and a nominal spring constant of 20 N/m. The images were acquired in dynamic tapping mode. In order to entirely cover the effective roughness pattern, the scan area was selected as $8.0 \times 8.0\ \mu$m. The sampling points were 512×512 pixels and the scan rate was set to 0.6 Hz. The topographic data were imported into Gwyddion software for image presentation and general processing (Nečas & Klapetek, 2012).

The tip shapes were characterized before and after the AFM measurements by high-resolution SEM imaging. The apex radius was estimated to be increased from 10 to 16 nm while the tip shank maintained its initial geometry. Considering the fact that the root mean square (rms) radius of each roughness artifact is at least one order of magnitude larger than the tip radius (Chen et al., 2014), the tip dilations are not severe. Furthermore, dilations induced by the tip shank, but not the apex, are possibly the dominant geometric coupling under our experimental conditions. Consequently, the effective tip size could be approximated as unchanged in acquiring the topographic data, though tip dilations remain. That is to say, the slight tip wear could be reasonably neglected in the following data analysis.

The optical nano measurements were carried out on a 3D confocal LSM (VK-X210, Keyence Corporation, Osaka, Osaka-fu, Japan). This microscope is able to acquire surface data with a deep depth of field and high contrast in a wide range of magnifications up to 24,000×. The resolution in the vertical direction can reach almost sub-nanometer scale. The laser wavelength was 408 nm and numerical aperture of the objective lens 0.95. The LSM was operated at a 150× objective magnification, a 20× eyepiece magnification, and an 8× optical zoom magnification. Each image was acquired in a rectangular area of $1{,}024 \times 768$ pixels with a calibration constant of 11.456 nm/pixel. Surface data of the effective roughness area were extracted and also imported into the Gwyddion software for image representation. A subtraction of the flat base plane was applied as only the relative surface height variations were of concern.

Spectral Analysis

PSD analysis, which can describe the roughness characteristics at each length scale, is a powerful tool for global

characterization of surface topography (González Martínez et al., 2012). The 2D PSD is given by the squared modulus of the Fourier transform of topography $z(x,y)$, or equivalently, the Fourier transform of the ACF (Wu, 2002):

$$P_C(\omega_x,\omega_y)=\frac{1}{4\pi^2}\int_{-\infty}^{\infty}\int_{-\infty}^{\infty}R(x,y)\times\exp[-i(\omega_x x+\omega_y y)]dxdy, \tag{2}$$

where ω_x and ω_y are the spatial frequencies in the x and y directions. Note that the above expression is not restricted to only positive frequencies. In the spectral evaluation of a roughness surface, one common approach is to calculate the PSD of each sectional profile and then averaging all the spectra (González Martínez et al., 2012). However, the surfaces here are isotropic and averaging in all angular directions is more reasonable. To do this, transformations from Cartesian to polar coordinates are first applied:

$$\begin{aligned}\omega_x&=\omega\cos\psi,\\ \omega_y&=\omega\sin\psi.\end{aligned} \tag{3}$$

Then, the 2D PSD is rewritten in a polar coordinate as:

$$P_P(\omega,\psi)=P_C(\omega\cos\psi,\omega\sin\psi). \tag{4}$$

Redefining the above PSD in a way that $\omega\geq 0$ and $\psi\in[0,2\pi)$, we can interpret $P_P(\omega,\psi)$ as containing the power owing to variations of the spatial frequency ω in a direction specified by the angle ψ. Finally, the 1D radial PSD is calculated by averaging over all angles (Ong et al., 2012):

$$P_R(\omega)=\int_0^{2\pi}P_P(\omega,\psi)\omega d\psi. \tag{5}$$

Spectral features of AFM and LSM measurements can be addressed from the above radial PSD analysis. For a reasonable hypothesis, the spectra may be divided into three different regions as schematically illustrated in Figure 1. For surface components whose spatial frequencies are below a critical frequency ω_L, the AFM or LSM measurements are accurate.

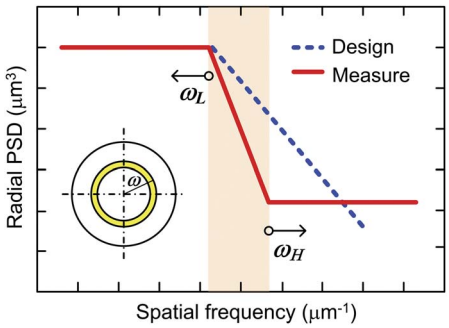

Figure 1. Illustration of the supposed spectral features of atomic force microscopy and laser scanning microscopy in characterizing the roughness surfaces. The measurement is accurate when $\omega<\omega_L$ with ω_L the critical spatial frequency, and it is dominated by the tip dilation where $\omega_L<\omega\leq\omega_H$. Noise is the main contribution when $\omega>\omega_H$. The inset schematically depicts calculation of the averaged radial power spectral density.

When the spatial frequency increases to larger than ω_H, the spectral power of the designed surface vanishes to a negligible value while the measured ones reach nearly constant magnitudes. In such a spectral domain, noise is the major contribution. For surface components whose frequencies are within the lower and upper limits defined by these two frequencies, that is, $\omega_L<\omega\leq\omega_H$, tip dilations are the dominant factors, inducing deviations in the PSD spectra. Note that either the solid tip of an AFM or the laser tip of a LSM has a finite size.

Results

Spectral Comparisons on Artifacts with Different Autocorrelation Lengths

The design and AFM and LSM images of the Gaussian roughness surfaces are shown in Figure 2. Here, the autocorrelation lengths at the 0.1 decay are 200, 320, 400, and 500 nm, respectively. For this series of surfaces, the rms roughness S_q, that is, the standard deviation of surface heights σ, is kept nearly constant. Several determinations can be made from the image comparisons. First, close correspondence of the major peaks or valleys is observable among the design, AFM, and LSM data. Second, the visual qualities of AFM images prevail against those of LSM, for which the scanned images are slightly blurred. Third, agreement among the design, AFM, and LSM images of surfaces with a larger autocorrelation length are better. Last, the peak-to-valley surface heights obtained by LSM are larger than the ones measured by AFM and the respective designed values for all of the patterns, which are depicted in the color bars of the shaded topography images.

For quantitative evaluations, spectral characteristics are mainly considered and the results are presented in Figure 3. We find that the calculated radial PSD is in exactly the supposed form as illustrated in Figure 1. In principle, the critical frequencies or wavelengths can be determined from the averaged radial PSD spectra. However, these PSD curves have obvious local variations. So the judgements of the critical frequencies may fail to be reliable and stable enough. To solve this problem, the PSD spectra are integrated and then normalized:

$$P_{RCN}(\omega)=\frac{\int_0^{\omega}P_R(\tilde{\omega})d\tilde{\omega}}{\int_0^{\infty}P_R(\tilde{\omega})d\tilde{\omega}}. \tag{6}$$

The normalized cumulative radial PSD is much smoother and the power increases with increase in the spatial frequency. The critical frequency ω_L can be therefore obtained unambiguously. Here, we apply the criterion that 95% of the total spectral power is reached at the critical cut-off frequency (see Fig. 3b). The corresponding critical wavelength is denoted as λ_L. Surface components whose wavelengths are larger than λ_L are considered to be effective. In other words, they are not severely distorted (Lee & Cho, 2012). Moreover, the normalized cumulative PSD spectra of the design surface, AFM, and LSM measured images become much more analogous to each other when the surface autocorrelation length increases. Comparatively, the

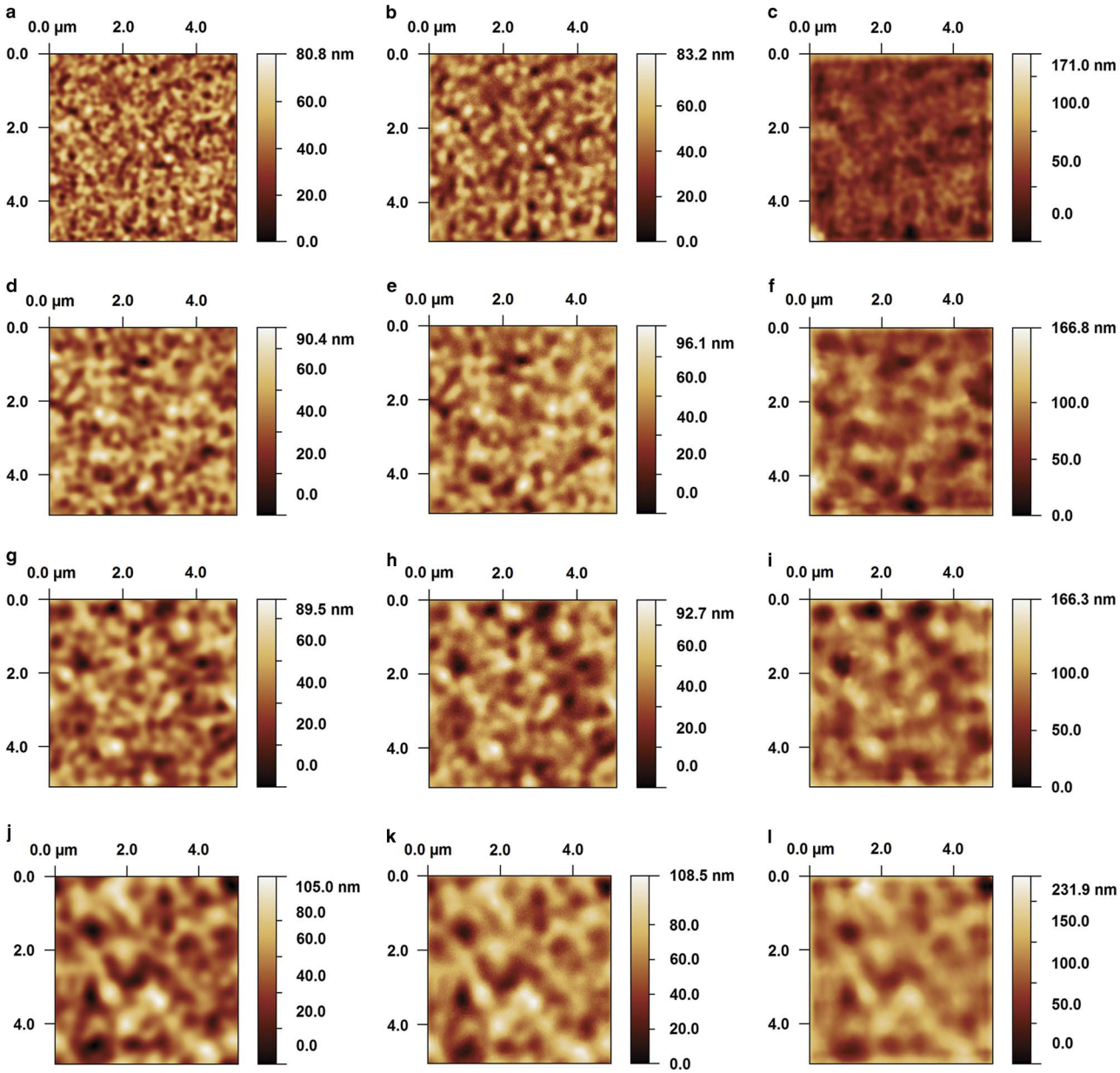

Figure 2. Design (left column), atomic force microscopy (middle column), and laser scanning microscopy (right column) images of the Gaussian roughness surfaces. **a–c:** Images of the surface with the autocorrelation length $\tau = 200$ nm, (**d–f**) $\tau = 320$ nm, (**g–i**) $\tau = 400$ nm, and (**j–l**) $\tau = 500$ nm.

spectra calculated from the AFM images are in better agreement with the designed ones as shown in Figure 3.

The critical wavelength as a function of the surface parameters of the series of Gaussian roughness patterns, namely the autocorrelation length and the surface height standard deviation, is plotted in Figure 4. The results demonstrate that the critical wavelengths determined from the design surface and the AFM data are in accordance. With the increase in autocorrelation length, the gap between designed and evaluated critical wavelengths decreases markedly from 11.2 to 3.6 nm. This phenomenon implies that AFM measurements on a sample surface with a large autocorrelation length are more accurate under the same conditions (Chen & Huang, 2009). The main distortion in AFM imaging is subsequently deduced to be caused by tip dilations. The critical wavelengths calculated from the LSM data are larger than the ones from the AFM data and the design surface. The increment relative to the theoretical value ranges from 18 to 48%. Furthermore, the intrinsic dependency on surface parameters in LSM seems not to be straightforward, which could be sensitive to various factors such as local surface gradient and multiple scattering (Gao et al., 2008).

Spectral Comparisons on Artifacts with Different Height Distributions

Now we analyze the artifacts with non-Gaussian surface height distributions. Structures with different skewness, but similar other statistical parameters, were generated and fabricated.

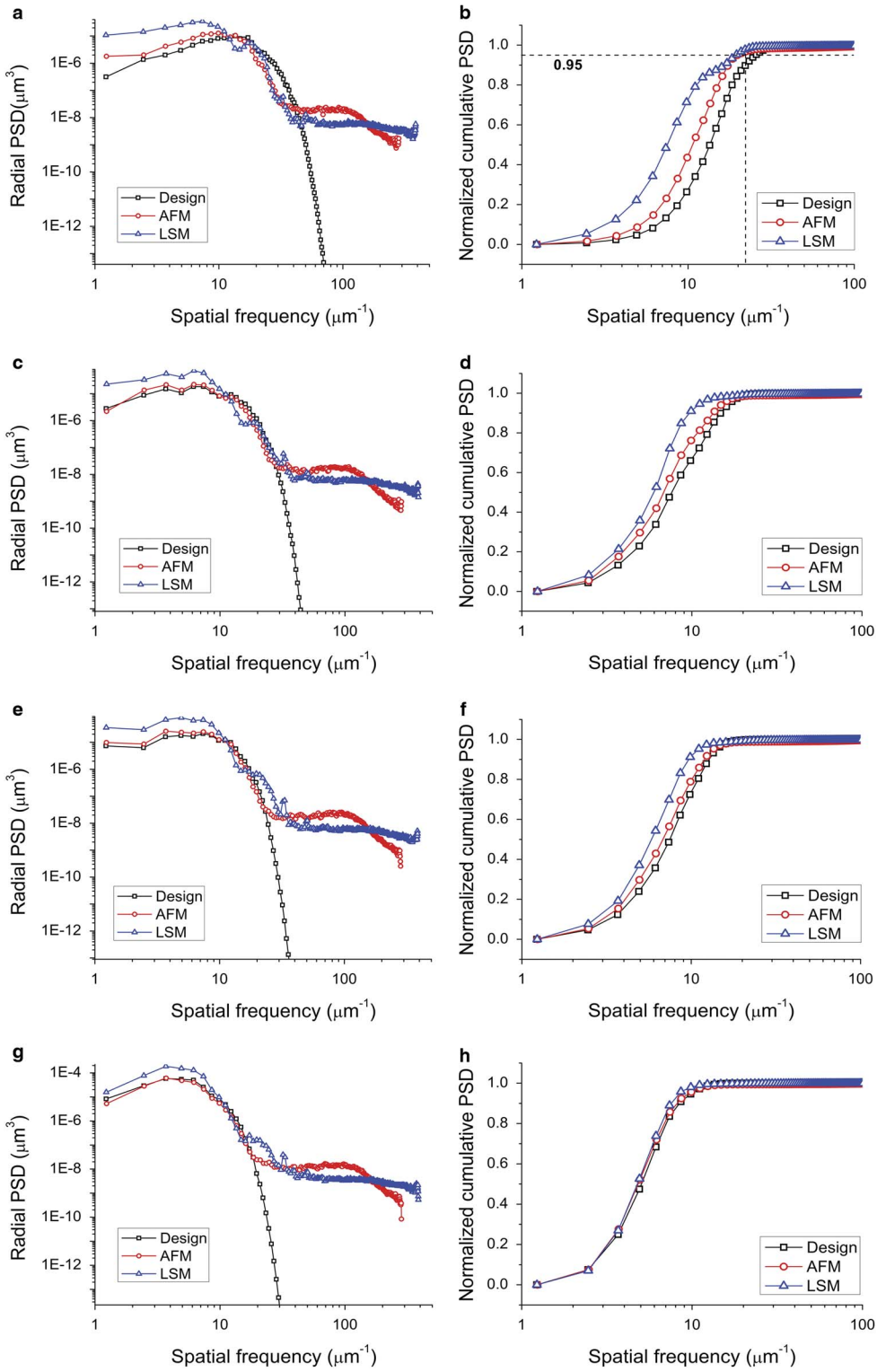

Figure 3. Radial power spectral density (PSD) (left column) and normalized cumulative radial PSD (right column) of the Gaussian roughness surfaces. **a–b:** The spectra for the surface with the autocorrelation length $\tau = 200$ nm, (**c–d**) $\tau = 320$ nm, (**e–f**) $\tau = 400$ nm, and (**g–h**) $\tau = 500$ nm.

The typical AFM and LSM images, which are only plane corrected, together with the design surfaces are illustrated in Figure 5. The skewnesses are 0, −1, and 1, respectively. The kurtosis is designed to be 5 and the autocorrelation length is 320 nm for each surface. From the results, the design, AFM, and LSM images are in well accordance. Measurements on Gaussian and negatively skewed surfaces are more accurate than those on positively skewed surfaces. More significant

probe tip dilations will be coupled in scanning a surface with a positive skewness where sharp peaks and flat valleys are the dominant structures. Again, the peak-to-valley heights obtained by LSM are larger than those scanned by AFM, and the LSM images are somewhat blurred.

The cumulative PSD spectra are shown in Figure 6. For the two surfaces with skewnesses of 0 and − 1, the PSD spectra of AFM data and design surface are in close agreement while the spectra of LSM data deviate obviously.

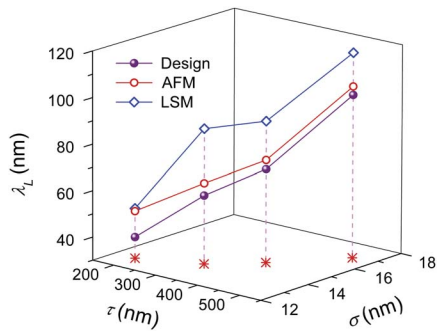

Figure 4. Critical wavelength λ_L as a function of the autocorrelation length τ and the standard deviation of surface heights σ.

For the surface with the positive skewness of 1, the three PSD spectra do not match so well, suggesting larger distortions in both AFM and LSM measurements. The critical wavelengths determined from the two surfaces with the skewnesses of 0 and − 1 are almost the same, within 2% relative deviations. They are about 59.5 nm for the design surfaces, 64.8 nm for the AFM images and 88.2 nm for the LSM images. However, the critical wavelengths calculated from the surface with the skewness of 1 are larger at 63.0 nm for the design, 78.9 nm for the AFM image, and 99.9 nm for the LSM image. Note that the designed critical wavelengths are not expected to have such obvious discrepancies among the three surfaces with different height distributions (Fig. 6d).

Impact on Surface Parameter Evaluations

According to the above analyses, the cut-off frequency of LSM is smaller and the power of the low frequency component is larger compared with AFM. These characteristics in the frequency domain mean that LSM can fail to distinguish certain subtle spatial features and surface height variations may be overestimated. For verification, quantitative evaluations of 3D roughness parameters were carried out. The representative results on the Gaussian surfaces are compared

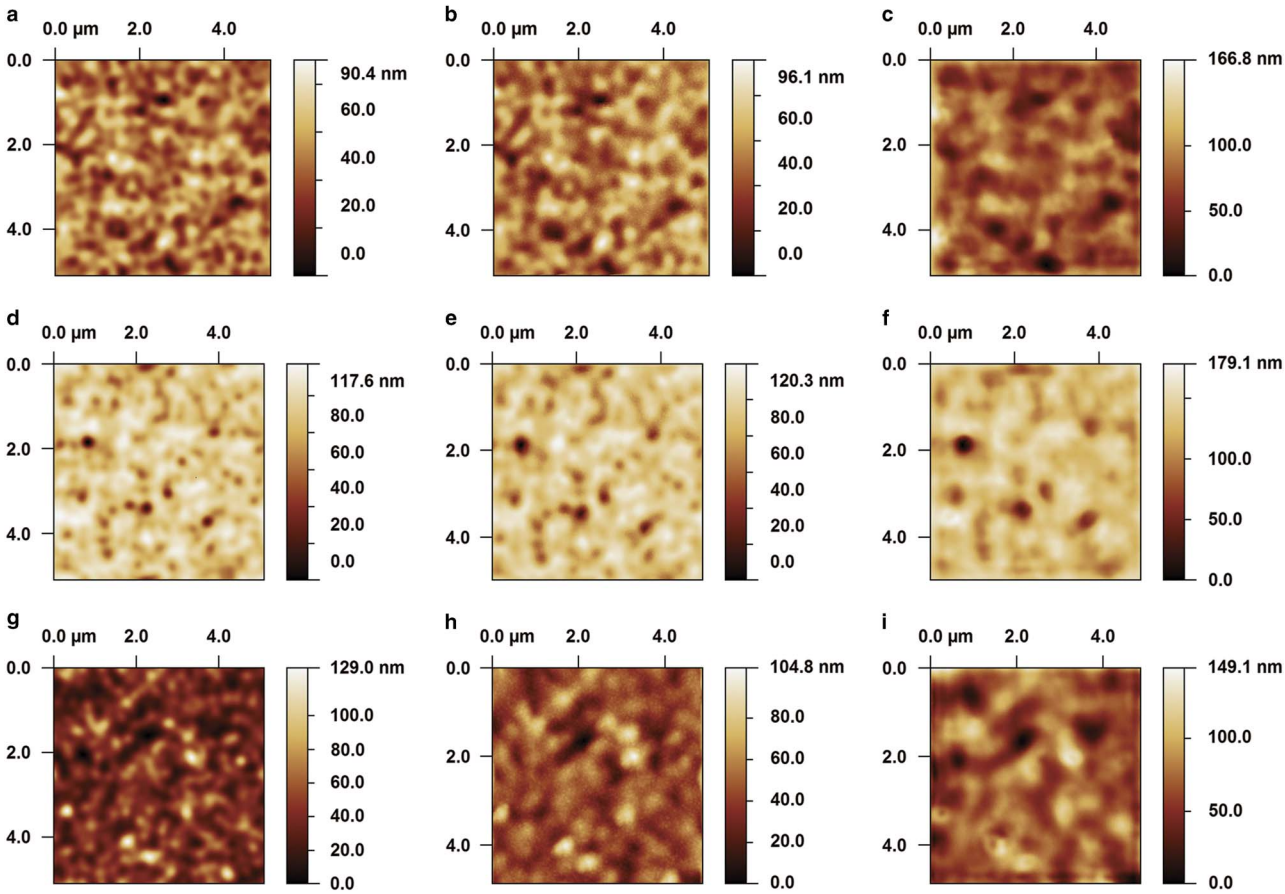

Figure 5. Design (left column), atomic force microscopy (middle column), and laser scanning microscopy (right column) images of the roughness surfaces with different height distributions. The surfaces have the same autocorrelation length of 320 nm. **a–c:** Images of the surface with skewness $S_{sk} = 0$, (**d–f**) $S_{sk} = -1$, and (**g–i**) $S_{sk} = 1$.

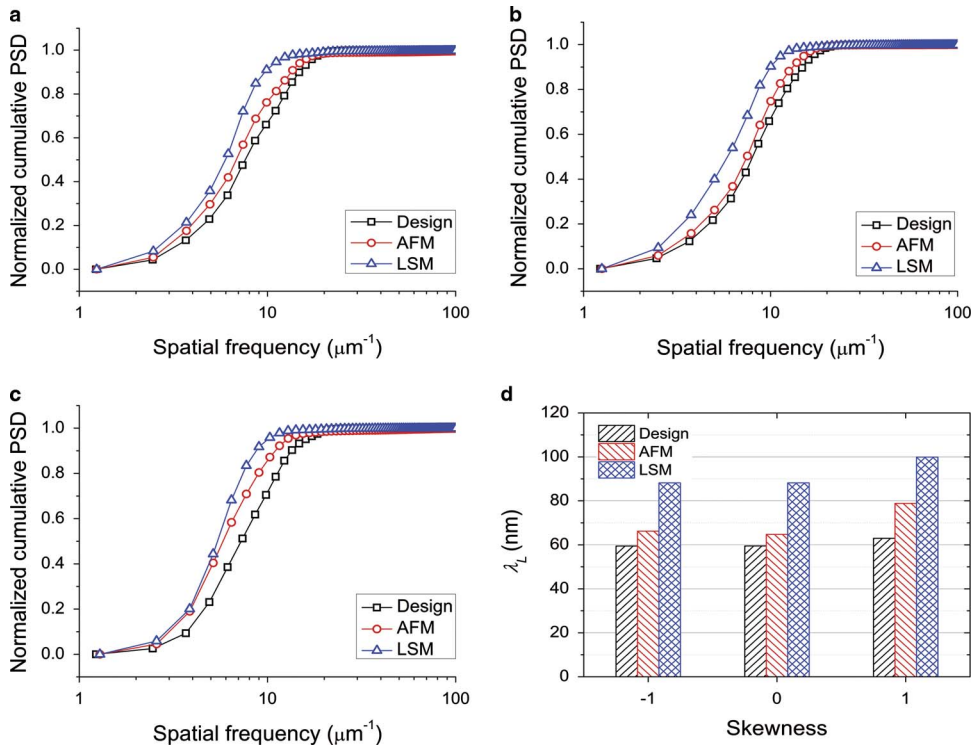

Figure 6. Spectral characteristics of the surfaces with different height distributions. The surfaces have the same autocorrelation length of 320 nm. **a**: Normalized cumulative radial power spectral density of the surface with skewness $S_{sk} = 0$, (**b**) $S_{sk} = -1$, (**c**) $S_{sk} = 1$, and (**d**) determined critical wavelengths from the design, atomic force microscopy, and laser scanning microscopy data sets.

in Figure 7. For clarity, we only present some typical parameters, namely the rms surface roughness S_q, skewness S_{sk}, autocorrelation length at the 0.2 decay S_{al20}, and rms surface slope S_{dq}. These four parameters are adopted to highlight the AFM and LSM acquired surface characteristics in terms of amplitude, height distribution, spatial property, and hybrid of amplitude and spatial properties.

For the parameter S_q, the measurement accuracy of AFM is satisfactory and the deviation relative to the expected value is within the range of − 6 to 7%. On the contrary, LSM overestimates the surface amplitude of each roughness pattern, with the increment in the range of 56–71%. For the parameter S_{sk}, the distributions are distorted a little by both measurement methods. Although the surface heights generally maintain their near-Gaussian forms, there is a slight tendency to turn into negatively skewed distribution because of the dilations of the sensing tip. The spatial length S_{al20} is always overestimated via either AFM or LSM. With the increase in autocorrelation length, the measured one becomes closer to the theoretically expected value owing to the reduced coupling of tip geometry. When the autocorrelation length reaches 500 nm, neither method generates an overestimation larger than 5%. As for the hybrid parameter S_{dq}, the determined value by AFM is accurate again, and the relative error is within 4% except for the surface with the smallest autocorrelation length. However, this parameter calculated from the LSM image has a large relative error, which ranges from 15 to 106%. The large deviations in LSM measurements of the amplitude and spatial properties subsequently induce huge errors in the slope characterizations.

Discussion

To further elucidate the differences and the main error sources in AFM and LSM measurements, it is necessary to recognize how the errors distribute in the entire scanned area. Toward this purpose, template matching was performed. The matching analysis can eliminate the influence caused by the fact that the coordinates of the design template and the measured data are not the same. In our approach, the template is fitted into a nonuniform rational B-spline surface and the matching is performed iteratively with the Levenberg–Marquardt algorithms (Jiang et al., 2010). Such a method has high accuracy and efficiency in metrological applications (Chen et al., 2013).

Matching results on typical data sets are presented in Figure 8. Here, the surface is the one with the autocorrelation length of 320 nm and the skewness of − 1. The measured topography data are plotted in the form of meshes while the residuals are overlaid on the surface for color rendering. In such a way, the domains where the heights are overestimated or underestimated can be clearly seen. The AFM results are precise and the residuals are near zero at most of the central positions of the local peaks. The residuals at the peak

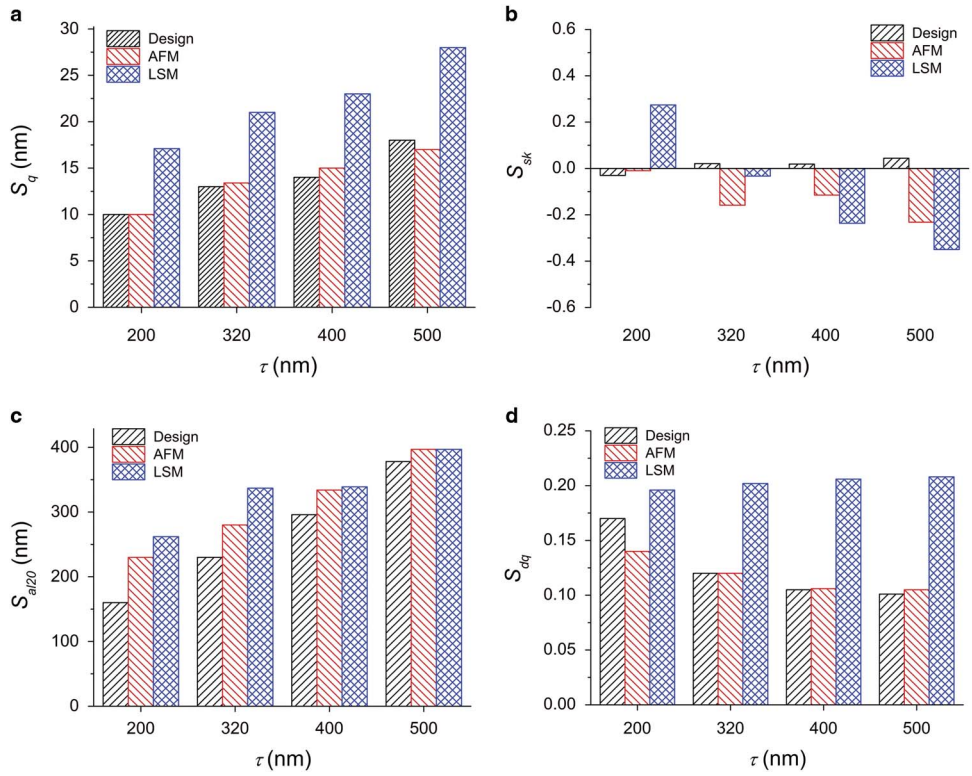

Figure 7. Surface parameter comparisons of four Gaussian surfaces whose autocorrelation lengths are 200, 320, 400, and 500 nm from left to right in each subfigure. **a:** Root mean square surface roughness S_q, (**b**) skewness S_{sk}, (**c**) autocorrelation length at the 0.2 decay S_{al20}, and (**d**) root mean square surface slope S_{dq}.

shoulders increase owing to tip dilations. In some of the valleys, the measured depth is even deeper than the designed one. However, these deviations occur most likely in fabrications but not measurements. The deepest valleys may be overbombarded. In the LSM characterizations, a large amount of peaks and valleys are overestimated. Comparatively, the extreme residual of AFM is smaller, which is in accordance with the evaluations of surface amplitude parameters.

In the meanwhile, the cut-off spatial frequency of LSM is smaller, which means that some tiny geometric features can fail to be distinguished. Figure 9 illustrates typical sectional profiles taken from nearly the same position in the design surface and the corresponding AFM and LSM images. We can find that the surface peak-to-valley heights are overestimated in LSM measurements, as illustrated in the left-side shaded region. Compared with the AFM data and the design surface, regions with high frequency surface components become indistinguishable, as illustrated in the right-side shaded region. The profile comparison also demonstrates that some local peak-to-valley heights measured by LSM are relatively accurate while others are obviously erroneous. Such results indicate that a simple scaling may fail to recover all of the surface parameters satisfactorily. The local slope/curvature-relevant features and the measurable wavelength have to be taken into consideration for precise scaling.

Generally, the interactions of the laser focal point and the surface geometry are rather complex issues, which involve different influencing factors such as surface gradient, material properties, and multiple scattering (Leach & Haitjema, 2010). Because of the complicities in quantitative LSM evaluations, further systematic experiments and modeling are still necessary. Nevertheless, the developed irregular roughness artifacts are believed to have potential use in exploring all of these subjects more quantitatively since the surfaces are digitally designed and fabricated with specified statistical parameters. Compared with other kinds of sinusoid or groove structures, such surface patterns can represent the actual surface areal roughness measurement situations more accurately. Moreover, the fundamental results here demonstrate that the developed roughness artifacts have well-defined mulitfrequency components, which are suitable for investigating the instrument responses at different spatial frequencies.

Conclusions

AFM and LSM measurements on specially designed surface areal roughness artifacts were performed and compared. Spectral analysis was adopted to characterize the measurement differences. In general, both AFM and LSM can image the fabricated roughness patterns with high 3D fidelity.

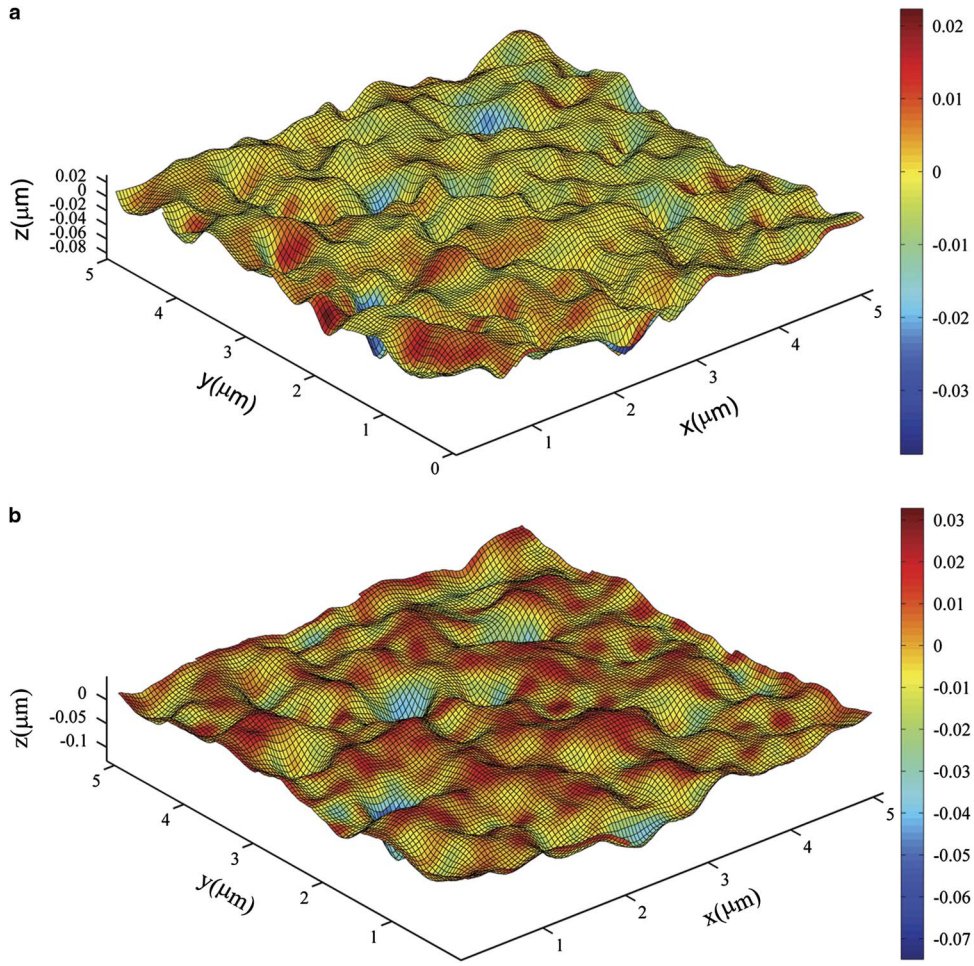

Figure 8. Typical residuals after template matching. Here the residual magnitudes are shaded on the measured surface data. The surface skewness is − 1 and the autocorrelation length is 320 nm, (**a**) atomic force microscopy result, and (**b**) laser scanning microscopy result.

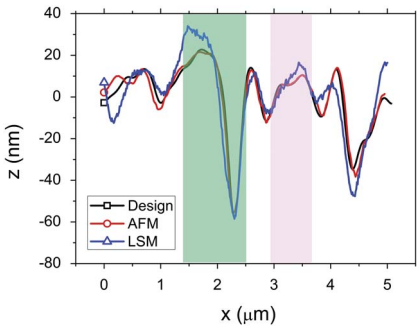

Figure 9. Comparisons of the sectional profiles of the design, atomic force microscopy, and laser scanning microscopy images. The profiles are taken at the same position.

When the surface autocorrelation length increases from 200 to 500 nm, the analyzed cumulative PSD spectra of all three data sets coincide well with each other. Compared with the AFM scanned result, deviation of the LSM image is obviously larger. The critical wavelength of AFM is smaller than LSM and it agrees better with the designed one. The gap between the measured and designed critical wavelengths is dramatically reduced with the increase in surface autocorrelation length. Measurements of the surface with a near zero or negatively skewed height distribution, together with a large autocorrelation length, are more accurate if other geometrical properties are similar. On the contrary, roughness characterizations of the surface with a positive skewness are greatly distorted owing to larger dilations of either the solid AFM probe or the LSM laser probe. The developed artifacts are able to provide reference nanostructures for characterizing the spatial frequency response of the microscopes.

The larger cut-off wavelength of LSM measurement indicates that the quantitative evaluations of surface parameters can be distorted at the nanometer scale. Results show that LSM overestimates the surface peak-to-valley height and the fastest decay autocorrelation length. Owing to these deviations, LSM characterizations of surface slope parameters have larger errors. Instead, AFM measurements of amplitude, spatial, and hybrid characteristics are satisfactory. Template matching analysis verifies that the main distortions in AFM characterizations can be attributed to tip dilations

while the influencing factors in LSM appear to be rather complex and the distortions are generally larger.

Acknowledgment

This work was supported by the National Natural Science Foundation of China (Nos. 51275503 and 91023021), and the "973" Project (No. 2011CB932801).

References

Bakolas, V. (2003). Numerical generation of arbitrarily oriented non-Gaussian three-dimensional rough surfaces. *Wear* **254**, 546–554.

Baršić, G., Mahović, S. & Zorc, H. (2012). Development of nano-roughness calibration standards. *Meas Sci Technol* **23**, 035009-1–035009-9.

Bonetto, R.D., Ladaga, J.L. & Ponz, E. (2006). Measuring surface topography by scanning electron microscopy. II. Analysis of three estimators of surface roughness in second dimension and third dimension. *Microsc Microanal* **12**, 178–186.

Botta, A.C., Duarte, S. Jr., Paulin Filho, P.I. & Gheno, S.M. (2008). Effect of dental finishing instruments on the surface roughness of composite resins as elucidated by atomic force microscopy. *Microsc Microanal* **14**, 380–386.

Brissonneau, V., Escoubas, L., Flory, F., Berginc, G., Maire, G. & Giovannini, H. (2012). Laser assited fabrication of random rough surfaces for optoelectronics. *Appl Surf Sci* **258**, 9171–9174.

Chen, Y. & Huang, W. (2004). Numerical simulation of the geometrical factors affecting surface roughness measurements by AFM. *Meas Sci Technol* **15**, 2005–2010.

Chen, Y. & Huang, W. (2009). Influences of geometrical factors on quantitative surface roughness evaluations by atomic force microscopy. *J Nanosci Nanotechnol* **9**, 893–896.

Chen, Y., Luo, T. & Huang, W. (2014). Focused ion beam fabrication and atomic force microscopy characterization of micro/nanoroughness artifacts with specified statistic quantities. *IEEE Trans Nanotechnol* **13**, 563–573.

Chen, Y., Zhang, X., Luo, T., Liu, X. & Huang, W. (2013). Fabrication and characterization of areal roughness specimens for applications in scanning probe microscopy. *Meas Sci Technol* **24**, 055402-1–055402-9.

Da Silva, M.A.B., Fardin, A.B., De Vasconcellos, R.C.C., Santos, L. M., Tonholo, J., Da Silva Júnior, J.G. & Dos Reis, J.I.L. (2011). Analysis of roughness and surface hardness of a dental composite using atomic force microscopy and microhardness testing. *Microsc Microanal* **17**, 446–451.

Fujita, D., Itoh, H., Ichimura, S. & Kurosawa, T. (2007). Global standardization of scanning probe microscopy. *Nanotechnology* **18**, 084002-1–084002-7.

Gao, F., Leach, R.K., Petzing, J. & Coupland, J.M. (2008). Surface measurement errors using commercial scanning white light interferometers. *Meas Sci Technol* **19**, 015303-1–015303-13.

González Martínez, J.F., Nieto-Carvajal, I., Abad, J. & Colchero, J. (2012). Nanoscale measurement of the power spectral density of surface roughness: How to solve a difficult experimental challenge. *Nanoscale Res Lett* **7**, 174-1–174-11.

Hanlon, D.N., Todd, I., Peekstok, E., Rainforth, W.M. & van Der Zwaag, S. (2001). The application of laser scanning confocal microscopy to tribological research. *Wear* **251**, 1159–1168.

Jiang, X., Zhang, X. & Scott, P.J. (2010). Template matching of freeform surfaces based on orthogonal distance fitting for precision metrology. *Meas Sci Technol* **21**, 045101-1–045101-10.

Jung, Y.C. & Bhushan, B. (2006). Contact angle, adhesion and friction properties of micro- and nanopatterned polymers for superhydrophobicity. *Nanotechnology* **17**, 4970–4980.

Kang, K.W., Pereda, M.D., Canafoglia, M.E., Bilmes, P., Llorente, C. & Bonetto, R. (2012). Uncertainty studies of topographical measurements on steel surface corrosion by 3D scanning electron microscopy. *Micron* **43**, 387–395.

Leach, R. & Haitjema, H. (2010). Bandwidth characteristics and comparisons of surface texture measuring instruments. *Meas Sci Technol* **21**, 032001-1–032001-9.

Lee, D.H. & Cho, N.G. (2012). Assessment of surface profile data acquired by a stylus profilometer. *Meas Sci Technol* **23**, 105601-1–105601-12.

Liu, K. & Jiang, L. (2011). Bio-inspired design of multiscale structures for function integration. *Nano Today* **6**, 155–175.

Liu, X., Luo, T., Chen, Y., Huang, W. & Piaszenski, G. (2012). Optimal design and fabrication of three-dimensional calibration specimens for scanning probe microscopy. *Rev Sci Instrum* **83**, 053708-1–053708-5.

Luo, T., Liu, X., Chen, Y., Huang, W. & Liu, Z. (2013). Design and laser fabrication of controllable non-Gaussian roughness surfaces at microscale. *Appl Surf Sci* **276**, 95–100.

Nečas, D. & Klapetek, P. (2012). Gwyddion: An open-source software for SPM data analysis. *Cent Eur J Phys* **101**, 181–188.

Nemoto, K., Yanagi, K., Aketagawa, M., Yoshida, I., Uchidate, M., Miyaguchi, T. & Maruyama, H. (2009). Development of a roughness measurement standard with irregular surface topography for improving 3D surface texture measurement. *Meas Sci Technol* **20**, 084023-1–084023-7.

Ong, D.C., Solanki, S., Liang, X. & Xu, X. (2012). Analysis of laser speckle severity, granularity, and anisotropy using the power spectral density in polar-coordinate representation. *Opt Eng* **51**, 054301-1–054301-7.

Persson, B.N.J., Albohr, O., Tartaglino, U., Volokitin, A.I. & Tosatti, E. (2005). On the nature of surface roughness with application to contact mechanics, sealing, rubber friction and adhesion. *J Phys Condens Matter* **17**, R1–R62.

Santos, R.P., Arruda, T.T.P., Carvalho, C.B.M., Carneiro, V.A., Braga, L.Q.V., Teixeira, E.H., Arruda, F.V.S., Cavada, B.S., Havt, A., De Oliveira, T.M., Bezerra, G.A. & Freire, V.N. (2008). Correlation between Enterococcus faecalis biofilms development stage and quantitative surface roughness using atomic force microscopy. *Microsc Microanal* **14**, 150–158.

Seah, M.P. (2013). Nanoscale roughness and bias in step height measurements by atomic force microscopy. *Meas Sci Technol* **24**, 035004-1–035004-12.

Uchidate, M., Yanagi, K., Yoshida, I., Shimizu, T. & Iwabuchi, A. (2011). Generation of 3D random topography datasets with periodic boundaries for surface metrology algorithms and measurement standards. *Wear* **271**, 565–570.

Wu, J.J. (2000). Simulation of rough surfaces with FFT. *Tribol Int* **33**, 47–58.

Wu, J.J. (2002). Spectral analysis for the effects of stylus tip curvature on measuring isotropic rough surfaces. *Meas Sci Technol* **13**, 720–730.

Yamazoe, S., Kohori, A., Sakurai, H., Kitanaka, Y., Noguchi, Y., Miyayama, M. & Wada, T. (2012). Laser beam scanning microscope and piezoresponse force microscope studies on domain structured in 001-, 110-, and 111-oriented $NaNbO_3$ films. *J Appl Phys* **112**, 052007-1–052007-6.